AN EXPLORATION OF NON-KINEMATIC EFFECTS IN FLUX TRANSPORT DYNAMOS

Dário Passos[1,2,3,♣]**, Paul Charbonneau**[2,♠]**,
Patrice Beaudoin**[2,♡]

Abstract

Recent global magnetohydrodynamical simulations of solar convection producing a large-scale magnetic field undergoing regular, solar-like polarity reversals also present related cyclic modulations of large-scale flows developing in the convecting layers. Examination of these simulations reveal that the meridional flow, a crucial element in flux transport dynamos, is driven at least in part by the Lorentz force associated with the cycling large-scale magnetic field. This suggests that the back-reaction of the field onto the flow may have a pronounced influence on the long term evolution of the dynamo. We explore some of the associated dynamics using a low order dynamo model that includes this Lorentz force feedback. We identify several characteristic solutions which include single period cycles, period doubling and chaos. To emulate the role of turbulence in the back-reaction process we subject the model to stochastic fluctuations in the parameter that controls the Lorentz force amplitude. We find that short term fluctuations provide long term modulations of the solar cycle and, in some cases, grand minima episodes where the amplitude of the magnetic field decays to near zero. The chain of events that trigger these quiescent phases is identified. A subsequent analysis of the energy transfer between large scale fields and flows in the global magnetohydrodynamical simulation of solar convection shows that the magnetic field extracts energy from the solar differential rotation and deposits part of that energy into the meridional flow. The potential consequences of this marked departure from the kinematic regime are discussed in the context of current solar cycle modelling efforts based on flux transport dynamos.

Keywords: Solar Cycle:Models, Sunspots:Magnetic Fields, Sunspots:Statistics

[1] Departamento de Física, Universidade de Évora, Colégio
António Luis Verney, 7002-554 Évora, Portugal
[2] Départment de Physique, Université de Montréal, C.P.
6128 Centre-ville, Montréal, Qc, Canada H3C-3J7
[3] CENTRA, Departmento de Física, Instituto Superior
Técnico, Av. Rovisco Pais, 1049-001 Lisboa, Portugal
♣ email: dariopassos@ist.utl.pt
♠ email: paulchar@ASTRO.UMontreal.CA
♡ email: beaudoin@ASTRO.UMontreal.CA

1. Introduction

The long phase of very low activity having separated sunspot cycle 23 from cycle 24 has been unusual in more than its duration (White *et al.*, 2011). Both the solar polar magnetic field and interplanetary magnetic field have reached record low values; the poleward propagating branch of the rotational torsional oscillations has failed to appear (Howe *et al.*, 2011); the solar F10.7 radio flux failed to track sunspot number in its usual manner (Tapping and Valdés, 2011); and the solar irradiance itself may have hit record low values (Fröhlich, 2011), although this latter point remains subject of debate as it hinges on the manner irradiance composites are constructed from the disparate datasets spanning 30 years of space-borne measurements.

This state of affairs has prompted a flurry of modelling activities, whereby various types of dynamo and surface magnetic flux evolution models have been used to design explanations for these various anomalies. Prominent among these explanatory frameworks have been the so-called flux transport dynamos, in which both the equatorward propagation of activity belts and poleward transport of surface fields leading to polarity reversal are ascribed to the conveyor-belt effect of the large-scale meridional flow believed to pervade the solar convective envelope (see Charbonneau (2010) for a review). That forced variations in the meridional flow speed, whether stochastic or persistent, can affect the cycle amplitude in such models has been known for many years, and many specific examples have been published (e.g., Charbonneau and Dikpati (2000); Bushby and Tobias (2007); Passos and Lopes (2008); Lopes and Passos (2009); Passos and Lopes (2011); Karak (2010). However, modelling specifically targeted at the cycle 23/24 minimum has produced some interesting novel results. For example, Nandy *et al.* (2011) have shown that an increase in the meridional flow speed in the rising phase of the cycle, followed by a decrease in the descending phase, could produce both a long minimum and a low polar field strength. Although this trend runs counter to observational inferences of the surface meridional flow (see Hathaway and Rightmire (2010); but also Basu and Antia (2010); Ulrich (2010)), the discrepancy may well be related to the development of a high-latitude counterrotating secondary meridional flow cell in the late descending phase of cycle 23, which in itself could yield a delayed onset for cycle 24 as well as low polar field strengths (see Jiang *et al.* (2009); Dikpati *et al.* (2010)).

At any rate, all of the aforecited calculations utilize dynamo and/or surface flux transport models in which the spatial form of the meridional flow and its time variation (if any) are specified *a priori*, sometimes on the basis of surface observations, sometimes not. Indeed, with some rare exceptions (e.g., Rempel (2006), Karak and Choudhuri (2011)) all flux transport dynamo models published to date operate in this kinematic regime, where the backreaction of the Lorentz force on the relevant flows —meridional circulation, but also differential rotation and small-scale turbulence— is altogether neglected or, at best, modeled using simple and *ad hoc* algebraic quenching nonlinearities acting on the model's large-scale flows and/or source terms. This poses severe limitations on the explanatory capabilities of such models.

Our aim here is to go beyond this kinematic regime and explore the impact of dynamical magnetic backreaction of the dynamo-generated magnetic field on the global properties of the dynamo itself. Towards this end we take advantage of recent global magnetohydrodynamical simulations of solar convection producing solar-like cycles in the large-scale magnetic field they generate (Ghizaru *et al.*, 2010; Racine *et al.*, 2011). In such simulations, the nonlinear interaction between flow and field

is treated in a dynamically consistent manner at all spatial and temporal scales resolved in the simulations. In principle, any variation of the meridional flow can then be retraced to its dynamical origin by a posteriori analysis of the simulation output.

The remainder of this paper is organized as follows. In §2, we first examine and analyze a simulation output to extract trends between variations of the azimuthally-averaged large-scale meridional flow and magnetic field. Guided by these findings, we turn in §3 to a well-validated low-order dynamo model to further explore the variety of behaviors that could potentially materialize through the backreaction of the Lorentz force on the meridional flow. In §4 we add stochastic forcing to this low-order model, and investigate the resulting patterns of amplitude fluctuations, as well as the occurrence of Maunder-Minimum-like epochs of strongly suppressed activity. Armed with the insight so gained, we conclude in §5 by returning to the simulation output, to better understand the ways in which this magnetic backreaction regulates the amplitude of cycles developing therein.

2. Spatiotemporal variations of meridional flow in simulations

In kinematic flux transport dynamo models, the absence of dynamical feedback on the flow by the Lorentz force implies that the magnetic field is passively driven by whatever large-scale flow has been prescribed; in other words, the flow drives the magnetic field, and this is precisely what is implied by the "conveyor belt" analogy often tagged to flux transport dynamos. Moving to a fully dynamical situation, with the Lorentz force feedback now included, opens the possibility that the large-scale magnetic field could drive the flow, rather than the other way around. So the first question to be addressed is: is the flow driving the field, or the field driving the flow? or some possibly spatiotemporally-dependent combination of these two effects?

In order to seek a first answer to this question, we analyze the output of one of the global MHD simulations of the solar convection zone produced by Ghizaru *et al.* (2010) using the MHD simulation code EULAG-MHD (Charbonneau and Smolarkiewicz, 2011). This code solves the anelastic magnetohydrodynamical equations in a thick, thermally-forced stratified fluid shell ($0.62 \leq r/R_\odot \leq 0.96$) rotating at the solar rate and convectively unstable in the upper two thirds of the domain ($0.718 \leq r/R_\odot \leq 0.96$). At the algorithmic level, these simulations utilize a non-oscillatory forward-in-time upwind advection scheme, which guarantees the nonlinear stability of field gradients developing down to the mesh cell size, which in the present context yields a maximally turbulent state on a given mesh size. This permits the use of a relatively small spatial mesh, and therefore allows very long integration times. In the simulations analyzed herein, all dissipative effects are delegated to the numerical scheme, with the exception of radiative diffusion which is explicitly included in the energy equation. One disadvantage of this so-called implicit large-eddy simulation approach is the difficulty to directly estimate the Reynolds numbers from the simulation output; for the simulations considered here, estimates based on turbulent energy spectra suggest values $\sim 10^2$ (Ghizaru *et al.*, 2010), with magnetic Prandtl number of order unity. Full details on algorithmic implementation and model setup are provided in (Charbonneau and Smolarkiewicz, 2011), to which we refer the interested reader.

The particular simulation we are using is computed on a relatively coarse spatial mesh, namely $128 \times 64 \times 47$ in longitude $\times$ latitude $\times$ radius, spans 3615 solar days (nearly 300 years), and exhibits a number of solar-like features, including: (1) buildup of a strong (few kG) toroidal magnetic component peaking at the base of the convective layers, (2) regular magnetic polarity reversals with a period in the range of 35–40 years, (3) well-defined surface dipole moment, with the surface field strongly peaked at high latitudes, (4) internal differential rotation characterized by equatorial acceleration, polar decceleration, and a thin, modest tachocline-like rotational shear layer immediately beneath the convective layers, (5) torsional oscillations superimposed on the mean differential rotation, with twice the magnetic cycle period and amplitudes of a few nHz.

These simulations are fully dynamical on all spatiotemporally-resolved scales. Their analysis by Racine *et al.* (2011) indicates that dynamo action therein can be understood as akin to the $\alpha^2 \Omega$ of mean-field theory, in which shearing by differential rotation and the turbulent electromotive force both contribute to the production of the large-scale axisymmetric toroidal magnetic component. This type of dynamo action differs in some important ways from what is usually incorporated in some of the kinematic flux transport dynamos commonly used nowadays to model —and even predict— various characteristics of the solar cycle: there are no emerging or decaying sunspots and active regions in these simulations, and therefore no Babcock-Leighton mechanism, so that the production of the poloidal large-scale magnetic component is wholly due to the action of the turbulent electromotive force. Nonetheless, these simulations do develop an axisymmetric large-scale meridional flow component throughout the convective layers and, as will be shown presently, this meridional flow components does show a well-defined pattern of spatiotemporal variations on the same period as the magnetic cycle. These numerical simulation data are thus well-suited to study the two-way interaction between large-scale fields and flows.

The first step is to extract the large-scale components of the magnetic field and flows from the simulation output. Following Racine *et al.* (2011), we associate "large-scale" with the axisymmetric components of the flow and field, e.g. for the flow:

$$\mathbf{U}(r, \theta, t) = \frac{1}{2\pi} \int_0^{2\pi} \mathbf{u}(r, \theta, \phi, t)\, \mathrm{d}\phi \ , \tag{1}$$

where each component of $\mathbf{u}$ is a four-dimensional data cube (three spatial dimensions plus time) returned by the simulation. Large-scale meridional circulation then corresponds to the r and θ-component of the large-scale flow $\mathbf{U}$. In Figure 1 we present meridional plots of the time averaged large scale toroidal component of the magnetic field, B_ϕ, rotational frequency $\Omega/2\pi = U_\phi/r \cos\theta$, with $\theta \in [-\pi/2, \pi/2]$ the latitude, and the meridional flow components U_θ and U_r over cycles 1, 3 and 5 (cycles with the same polarity).

As can be seen on panel A, in this simulation the axisymmetric large-scale magnetic field peaks at mid-latitude immediately beneath the core-envelope interface, where its toroidal component dominates. The meridional flow component (C and D) are dominated in equatorial regions by strong, persistent flow structures approximately aligned with the rotation axis. These represent the residual signature of a system of elongated convective cells, the presence of which is typical of these types of global simulations, whether magnetohydrodynamical or purely hydrodynamical (e.g., Brun *et al.* (2004), Miesch and Toomre (2009)). Because the associated convective

flow velocities are quite large, even upon zonal and temporal averaging they yield a residual signal that dominates the axisymmetric meridional flow at low to mid-latitudes. At mid- to high latitudes, on the other hand, one recovers a relatively strong (~ 1 m s^{-1}) surface poleward flow, as well as an equatorward return flow concentrated at the core-envelope interface. Nonetheless, the meridional flow structure is clearly more complex than the single-cell configuration typically used in most flux transport dynamos.

We pay special attention to the bottom of the convection zone at the latitudes where B_ϕ builds up to peak strength (near $58°$ in this simulation). We do this because in this region, B_ϕ is strongest and the Lorentz force influence should be more pronounced. Moreover, in this region the meridional flow is mainly oriented in the latitudinal direction ($|U_r|/|U_\theta| < 0.1$), and is akin to the return flow usually invoked in 2D flux transport models. Consequently, this region is perhaps most relevant for a comparative study between the behavior of U_θ and B_ϕ. Figure 2 shows the time evolution of U_θ and B_ϕ^2, our proxy to represent the solar cycle.

By subtracting a 1 year smoothed signals from the original data, i.e., subtracting the black curves from the gray curves in Figure 2, we define the fluctuating components of the signals. The ratio between the rms power of the smoothed $\overline{U_\theta}$ and its fluctuations U_θ' reaches 29% here. Individual fluctuations with amplitude as high as 60% can be frequently identified in this longitudinally averaged velocity component, and even much higher at individual grid points. This is hardly surprising, given that the speeds characterizing the large-scale meridional flow are much lower than those associated with turbulent convection in this simulation, as in the sun. For the magnetic field, at this location this rms ratio is much smaller, at the 10% level.

An interesting point arises when we plot the evolution of B_ϕ^2 and U_θ side by side (top panel of Figure 3). The two quantities follow the same general pattern with U_θ lagging behind B_ϕ^2, most easily seen here in the N-hemisphere. A lag analysis reveals a small average lag of about 5 years. This lag suggests that the field at the base of the convection zone is modulating U_θ, rather than the other way around, i.e., the opposite of what is implicitly assumed in the kinematic dynamo regime.

We also examine several relations between cycle amplitude (defined by the value of B_ϕ^2 at cycle maximum), cycle period (time between two minima) and meridional flow amplitude (given by the maximum U_θ amplitude near cycle maximum). This is done separately for the two hemispheres at the latitudes and depths previously mentioned for the 6 half-cycles present in the simulation. The results are shown in the bottom panels of Figure 3. The linear correlation coefficient between flow amplitude and cycle period is $r = -0.04$, that between cycle amplitude and flow amplitude is $r = 0.78$, and that between cycle amplitude and cycle period is $r = -0.58$. Note that the latter moderate anticorrelation is similar to the so-called Waldmeier rule characterizing the sunspot number record. The moderately strong correlation between cycle amplitude and flow speed (Figure 3D) suggests again a dynamical link between these two quantities. The near-zero correlation between cycle period and flow speed (Figure 3E) arises because both hemisphere show here an opposite pattern of correlation, but examination of another similar simulations indicate that this hemispheric pattern is not robust, and that very low correlation between meridional flow speed and cycle period is the rule rather than the exception in these simulations.

Measuring joint variations of the large-scale magnetic field and meridional flow at one specific location in the simulation domain evidently offers an incomplete picture

of the complex interaction between flow and field. In particular, in the simulation considered here, the cycling large-scale magnetic fields alters not only the speed of the meridional flow, but also its spatial topology, namely its structuring into large-scale circulation cells spanning a large fraction of the simulation domain. One particular noteworthy such alteration is the development, in the descending phase of the magnetic cycle, of high latitudes, counterrotating meridional flow cells. This is quite interesting, because good evidence exists for the similar development of high-latitude counterrotating cells on the solar surface (Dikpati *et al.*, 2010; Ulrich, 2010). Basu and Antia (2010) and González Hernández *et al.* (2011), using helioseismic data for a complete solar cycle, also found evidence of time dependent variations in the meridional flow in the subsurface layers of the Sun.

Interestingly, we do observe in the simulation the growth and disappearance of a counterrotating secondary meridional flow cells at high latitudes in the course of each magnetic cycle, with a spatiotemporal evolution showing some definite similarities with observationally-inferred patterns, as depicted on Figure 4. Panel (A) is a time-latitude diagram of the zonally-averaged magnetic component at the core-envelope interface ($r/R = 0.718$), taken to be the simulation's equivalent to a sunspot butterfly diagram. Panel (B) is a time-latitude diagram of the latitudinal velocity residual at the top of the simulation domain ($r/R = 0.96$). This is obtained by subtracting from the latitudinal component of the velocity returned by the simulation the zonal and temporal average flow component over the full extent of the simulation. Notice, between ± 50 and 75 degrees latitude, the periodic alternance of regions of acceleration (yellow) and decceleration (blue) with respect to the mean, at a frequency twice that of the magnetic cycle. The peak amplitude of this oscillation is ~ 2 m s^{-1}, i.e. it exceeds the mean surface poleward speed at this latitude (~ 1 m s^{-1}, cf. Figure 1) by a factor of about two; in other words, starting near cycle maximum and throughout the descending phase of the magnetic cycle the surface flow becomes equatorward at these latitudes, reaching as far equatorward as 60 degrees latitude in the later stage of the descending phase of the cycle. The bottom panels on Figure 4, from (C) to (E), shows a series of snapshots of zonally-averaged meridional flow vectors near the North pole in the simulation, equidistant in time and collectively spanning the second magnetic half-cycle (as indicated by vertical line segments on panel A), plotted in a cartesian radius-latitude plane for clarity. At the time of polarity reversal ($t = 60$ yr) the zonally-averaged meridional flow is characterized by a strong downflow in polar regions, with a generally poleward surface flow and equatorward return flow at the core-envelope interface. Near the peak of the cycle ($t = 70$ yr) the polar downflow has reversed in the outer half of the convective layers, and a strong subsurface equatorward flow has begun to build up above 60 degrees in latitude. Halfway through the descending phase of the cycle ($t = 80$ yr) the primary surface flow is equatorward above 70 degrees latitude, and the subsurface meridional meridional flow has essentially vanished at all depths at high latitudes. Note however that at all times, a generally equatorward return flow remains present at and immediately beneath the core-envelope interface. Clearly, the reversal of the surface latitudinal flow is not a mere surface phenomenon, but is associated with changes in the zonally-averaged meridional flow extending deep into the convecting layers.

A precise and physically meaningful comparison of these results to surface observations of cycle-related variations in the meridional flow is unfortunately hampered by the fact that the simulation domain here extends only out to $r/R = 0.96$. The

anelastic approximation does break down in the subsurface layers, but the primary constraint here is of a practical computational nature: we simply cannot afford the very large number of grid points that would be required to capture the rapid outward decrease in density in the last few percent of the sun's radius, with the associated horizontal size reduction of convective cells it would produce due to the rapidly decreasing scale height. Nonetheless, the simple analysis carried out in this section indicate already that the meridional flow responds dynamically to the evolving large-scale magnetic field, and that the amplitude of this response is quite large. One can then wonder whether these variations in the meridional flow have an impact on the operation of the magnetic cycle itself. We now turn to this question.

3. Modified LODM

The fact that we observe a clear modulation from the magnetic cycle into the meridional flow, particularly obvious on both Figures 2 and 3, suggest that there may be feedback on the dynamo itself; this then raises a host of questions regarding the possible long term evolution of such a system, subjected to two-way dynamical coupling. This could be particularly important in dynamo models relying on the meridional flow to couple spatially distinct source regions, such as most current Babcock-Leighton solar cycle models operating in the advection-dominated regime.

In order to make a first exploration of the impact of this interaction on the long term dynamics of a flux transport dynamo, we modify the low order dynamo model (LODM) developed by Passos and Lopes (2008), Passos and Lopes (2011) to incorporate a magnetic field-dependent meridional flow. This low order model allows us to fully isolate the global aspects of the dynamical interactions between the meridional flow and magnetic field.

The model itself is a truncated version of the axisymmetric flux transport dynamo equations (Charbonneau, 2010), including Ohmic dissipation, shearing by differential rotation, as well as transport and shearing by meridional circulation. The truncation procedure is described at length in Passos and Lopes (2011), to which we refer the reader for all technical details. In brief, a dimensional approach is used to collapse all spatial dependencies by substituting $\nabla \rightarrow 1/\ell_0$, where ℓ_0 is a specific length of interaction for the large scale magnetic fields, usually taken in the range $\ell_0 \in [0.01R_\odot, 0.3R_\odot]$. The key assumption implicit in this spatial reduction is that there exist a single length scale ℓ_0 that properly characterizes the spatial variations of both large-scale flows and magnetic field. The model also incorporates an explicit magnetic buoyancy loss term as a limiting growth mechanism for the toroidal field when dynamo action is achieved. In this LODM the temporal evolution of toroidal and poloidal components of the solar magnetic field (B_ϕ and A_p) is given by

$$\frac{\mathrm{d}B_\phi}{\mathrm{d}t} = \left(c_1 - \frac{v_p(t)}{\ell_0}\right)B_\phi + c_2 A_p - c_3 B_\phi^3 , \qquad (2)$$

$$\frac{\mathrm{d}A_p}{\mathrm{d}t} = \left(c_1 - \frac{v_p(t)}{\ell_0}\right)A_p + \alpha B_\phi . \qquad (3)$$

The "structural coefficients" c_n are given by

$$c_1 = \frac{\eta}{\ell_0^2} - \frac{\eta}{R_\odot^2} , \qquad (4)$$

$$c_2 = \frac{R_\odot \Omega}{\ell_0^2} \; , \tag{5}$$

$$c_3 = \frac{\gamma}{8\pi\rho} \; , \tag{6}$$

where $R_\odot$ is the solar radius, v_p is an average speed for the meridional circulation, Ω represents an average differential rotation of the Sun, η is a mean magnetic diffusion in the SCZ and the term c_3 is defined by γ, a magnetic buoyancy loss rate and an average density, ρ, for the SCZ. As usual the regeneration mechanism from toroidal to poloidal field is represented by α. These c_n coefficients contain all the structure parameters in the model (e.g. rotation, buoyancy, magnetic diffusion, etc.), hence their name.

By using this LODM (working in the kinematic regime) and by comparing it to a magnetic field proxy constructed from the sunspot number time series, Passos and Lopes (2008), Passos (2011) inferred variations in the amplitude of the meridional flow for the past three centuries. Forcing complex 2.5D kinematic axisymmetric flux-transport models such as the Surya dynamo code (Chatterjee *et al.*, 2004) with this variation profile leads to very solar-like cycle amplitude fluctuation patterns (Lopes and Passos, 2009). Independent experiments with the Surya code by Karak (2010) also reveal a similar relation between flow and cycle amplitude.

We now assume that our large-scale meridional circulation, v_p, is divided into a "kinematic" constant part, v_0, due to angular momentum distribution and a time dependent part, $v(t)$, that is affected by the feedback of the magnetic field. Since the Lorentz force is highly dependent of the topology of the magnetic field, within this LODM we can only assume that this feedback term will depend on both components of the magnetic field. Therefore we redefine $v_p(t) = v_0 + v(t)$ where the time dependent part evolves according to

$$\frac{\mathrm{d}v(t)}{\mathrm{d}t} = a\, B_\phi A_p - b\, v(t) \; . \tag{7}$$

In this expression, the first term is a magnetic nonlinearity representing the Lorentz force and the second is a "newtonian drag" that ensures exponentially decay of $v(t)$ towards its imposed kinematic value v_0 in the absence of magnetic fields. From a dynamical point of view, this amounts to assuming that the Lorentz force associated with the cyclic large-scale magnetic field acts as a perturbation on the otherwise dominant, steady hydrodynamical quasi-balance between buoyancy and Reynolds stresses driving the meridional flow in the absence of magnetic fields. This approach to magnetic backreaction on large-scale flows has been used extensively already to model magnetically-mediated variations of differential rotation in mean-field dynamo models (see, e.g., Tobias (1996); Moss and Brooke (2000); Brooke *et al.* (2002), Bushby (2006)).

The system of equations (2-3) and (7) defines a simplified but non-kinematic flux transport dynamo model, in that it incorporates a dynamical feedback of the magnetic field on the meridional flow. As shown in Figure 5 for one cycle of a typical solution, the formulation proposed for v_p satisfies basic observational requirements, i.e., the amplitude of the flow component influenced by the Lorentz force, $v(t)$ varies in phase with the toroidal field (as observed in the 3D MHD simulation) while the amplitude of the complete meridional flow v_p follows the observational behavior and varies in anti-phase with B_ϕ (v_p grows in amplitude as B_ϕ approaches zero).

Although all spatial dependencies have been integrated away, the sign change of v_p near solar maximum can be related to the appearance of a high latitude counter-rotating cell. From a purely mathematical point of view (viz. eqs. (2) and 3)), in this model the meridional flow with negative values behaves as a source term and with positive values behaves as a sink term. The decrease in the amplitude of v_p during the rising phase of the cycle provides an extra quenching mechanism for the magnetic field growth.

This system presents a wide range of behaviors, according to the values chosen for the various numerical coefficients. The values used for the structure parameters, c_n, are taken from Passos and Lopes (2008), where the authors fit the LODM to a B_ϕ proxy data derived from the sunspot number. With these values the solution of the model reproduces the main features of the solar cycle (polarity reversals, cycle period, etc.). The focus now turns to the parameters associated with the meridional flow evolution, a, b and v_0. These coefficients will have a major role in the evolution of the solution space, as exemplified in Figure 6 where a few examples of solutions obtained using different values for these parameters are presented.

The initialization parameters (common to all calculations) are $B_\phi(0) = 0.1$, $A_p(0) = 0.1$ and $v(0) = 0.0$, which ensures that we start from a weak seed magnetic field and that the time dependent part of the flow is null. For the standard kinematic solution (panel (A) of Figure 6), the maximum amplitude of the cycles saturates after 70 years while for the non kinematic solution (second panel) this requires around 160 years. We also find that this initial transient depends nonlinearly on a and b. For example for fixed $a = 0.1$ the smaller the drag term b is, the longer it takes for the system to stabilize.

Behavior observed range from fixed-amplitude oscillations closely resembling kinematic solutions (cf. top and second panels), multiperiodic solutions (third panel), and even chaotic solutions (bottom panel). In order to better visualize these chaotic regimes and the manner in which they arise, we construct analogs of classical bifurcation diagrams by plotting successive peak values of cycle amplitudes, in sequences of solutions with fixed (a, v_0) combinations but increasing values of the drag parameter b. The result of this procedure is shown in Figure 7 for four such sequences. For certain (a, v_0) combinations, while sweeping through b, the system undergoes transition to and from chaos via series of classical period doubling bifurcations. Transition to chaos through bifurcations are also observed when holding b fixed and varying a instead. The range of dynamical behaviors accessible to this simple dynamical system is obviously quite rich.

4. Fluctuations and intermittency

In section (2) we verified that both the magnetic field and the flow exhibit significant amplitude fluctuations. Since the feedback of the magnetic field on the flow takes place in a very turbulent environment, it is plausible to assume that the parameter a, the one which controls the influence of the Lorentz force, could be subjected to stochastic variations.

To simulate this scenario we add to a a piecewise constant perturbation δa extracted from a zero-mean bounded uniform distribution $\delta a \in [-\Delta a, \Delta a]$, with a new updated value for δa generated at a cadence τ corresponding to the coherence time

of the fluctuations. We choose this coherence time to be one year, i.e. much smaller than the length of the cycle. Afterwards the LODM is solved under this stochastic forcing of a.

4.1. Modulation of cycle amplitude

As a result, and depending on the range of fluctuations, we see that the short term stochastic kicks in the Lorentz force amplitude create long term modulations in the amplitude of the cycles (hundreds of years). Panel B of Figure 8 shows clearly that even with a coherence time much shorter than the cycle period, cycle amplitude modulation patterns spanning many cycles nonetheless develop, including relatively frequent Dalton-Minimum-like episodes of reduced cycle amplitude lasting a few cycles (e.g., at $t \simeq 11210$, 11970, 12125, and 12280).

In order to produce better statistics, we extended the simulation of Figure 8 to 240000 years. The power spectrum of this simulation is shown in black on Figure 9, together with the equivalent power spectrum for a parent simulation (in gray) without stochastic forcing of the parameter a, but otherwise using the same numerical values for the other model parameters. The stochastically-forced solution has a mean period of of 10.2 years, a little lower than the 11 years characterizing the constant-a solution. The amplitudes of higher frequency harmonics decrease similarly with increasing frequency in both spectra, indicating that the shape of the cycles is not strongly affected by the fluctuations. The most significant difference between the two spectra is the presence, in the stochastically forced solution, of an extended low-frequency tail characterized by a broad bump around 56 yr period, the spectral manifestation of the multi-cycle amplitude modulation already visible on Figure 8.

4.2. Intermittency and Grand Minima

This stochastically-forced solution also exhibits intermittency, namely temporally extended epochs where cycle behavior ceases and the magnetic field falls close to zero. Panel C of Figure 8 shows one such episode. The duration and frequency of these long quiescent phases, where the magnetic field decays to very low values, is determined by the level of fluctuations of a and the value of b. The stronger this drag term b is, the shorter the minima are. At fixed value of b, the higher the level of fluctuation of a, the more frequent intermittency episodes become.

Figure 8 show a solution example computed over 40000 years that exhibits all the behaviors described before. For this example we used $a \in [0.01, 0.03]$ which corresponds to a $\Delta a/a = 0.5$ fluctuation level relative to its mean value (0.02), $b = 0.05$ and $v_0 = -0.11$. In this parameter range, the parent solution without stochastic forcing operates in the single period regime. Therefore, the fluctuations observed in this solution are a direct consequence of the stochastic forcing of the Lorentz force, rather than arising from excursions in the chaotic regime produced by random changes in the numerical value of a. For the same mean value of $a = 0.02$, the fluctuations threshold below which we do not detect intermittency episodes (in a 40000 years interval) is around $\Delta a/a = 0.45$. The systematic study needed to establish the variations of this intermittency threshold across the model's parameter space is beyond the scope of this paper, but the exploration we have carried out to date indicate that intermittency occurs over a broad portion of parameter space.

The characterization of these grand minima episodes is of obvious interest. Using the record of annual averaged sunspot number, we calculated the ratio between cycle maximum and cycle minimum. The mean value found for the complete time series indicates that the sunspot number at solar minimum is $\sim 4.5\%$ of its value during solar maximum. On this basis, we assume that this threshold can be extrapolated to the toroidal field and we look for time intervals in our simulation where B_ϕ falls below 4.5% of its average peak amplitude. We define a grand minimum when this period of low activity is longer than 11 years, as on Figure 8C. Based on this criteria we can investigate the statistical characteristics of these grand minima. Figure 10A identifies the moment and duration of grand minima episodes in this long simulation. The heights of the vertical bars indicate the duration of the minima. No obvious periodicity or other temporal pattern jumps to the eye here. This is confirmed upon computing the frequency distribution of grand minima duration (Panel B) and of inter-minima wait-times (Panel C), the latter being defined as the time interval elapsed between the end of a grand minimum and the onset of the subsequent one. That frequency distribution is compatible with an exponential form, as expected from a memoryless stationary random process. Also noteworthy on Figure 10B, the durations of grand minima cluster around integer multiples of the base period. This indicates that the phase coherence of the underlying cycle is preserved throughout grand minima. This behavior is compatible with the cosmogenic radioisotope record, which indicates that during the Maunder minimum, cyclic magnetic activity still took place, despite the dearth of sunspots (Beer *et al.*, 1998).

In this specific simulation we obtained 67 grand minima episodes. Although the average time between these events is of approximately 3500 years, the distribution of the "normal solar activity" in these inter-minima wait-times range from a couple of cycles to several millennia. As mentioned before, for a different (a, b, v_0) set, these distributions could take very different forms. In particular, increasing b reduces the recovery time, and therefore tends to shorten the duration of grand minima, with the opposite behavior when b is instead reduced. This behavior is similar to that observed by Brooke *et al.* (2002), who used a dynamical formulation similar to eq. (7) herein to model the magnetic backreaction on differential rotation, with their Prandtl number equivalent to our b parameter; in both models, the numerical value of these parameters sets the dynamical recovery time to "normal" cyclic behavior.

4.3. Phase space behavior

It is also interesting to look at the phase space $\{B_\phi,\ A_p,\ v_p\}$ to see how these quantities vary in relation to each other and try to understand what chain of events might trigger the grand minima episodes. Using the solution presented in Figure 8 we built the several phase spaces shown in Figure 11. The standard solution for the LODM without stochastic forcing, i.e. with a fixed at the mean value of the random number distribution used, is a limit cycle attractor, i.e., a closed trajectory in the $\{B_\phi,\ A_p\}$ phase space. This curve is represented as a black dashed trajectory in the panels of Figure 11. The gray points in this figure are the stochastic forced solution values sampled at a 1 year cadence. These points scatter around the attractor representing the variations in amplitude of the solution. Occasionally, the trajectories defined by these points collapse to the center of the phase space indicating a decrease in amplitude of the cycle, i.e. a grand minimum. The point $\{0,0\}$ is also another natural attractor of the system. The colored trajectory evolving in time from dark

red to yellow represents one of those grand minima, specifically that seen on Fig. 8C. The onset occurs when the solution is at a critical distance from the limit cycle attractor and gets a random kick further away from it. This kick makes the field grow rapidly. In turn, since the amplitude of the field grows fast, the Lorentz force will induce a similar growth in $v(t)$ eventually making v_p change sign. When this occurs, v_p behaves as a sink term quenching the field growth very efficiently. This behavior is seen in the two bottom panels of Figure 11 where we can see v_p decaying to it imposed "kinematic" value v_0 after the fields decay. After this collapse of v_p to v_0, the latter starts behaving has a pure source term again, and cyclic activity eventually resumes.

An interesting prediction can therefore be made in association with the specific manner in which the model enters such grand minima phases. As shown on Figure 11, onset takes place through a large excursion away from the attractor, which then implies higher-than average cycle amplitudes in the few cycles preceding collapse onto the $A_p = 0, B_\phi = 0$ axis in phase space. That this is indeed the case is readily apparent on Figure 8C. Under this specific form of intermittency, onset of grand minima should then be preceded by a few increasingly higher-than average cycles, with onset then taking place abruptly, while recovery is more gradual. This pattern of rapid onset and slow recovery is in fact compatible with inferences made on the basis of sunspot observations before and after the Maunder Minimum.

5. Concluding remarks: implications for solar cycle modelling

In this paper we have examined the dynamical interplay between a dynamo-generated large-scale magnetic field and large-scale meridional flows. We have done so using numerical output from global MHD simulations of solar convection, as well as from a simple low-order dynamical model obtained from spatial truncation of the axisymmetric mean-field dynamo equations, augmented by a nonlinearly coupled evolutionary equation for the meridional flow amplitude. The former is computationally expensive, but geometrically more realistic and dynamically consistent at all numerical resolved scales, while the latter allows very efficient exploration of parameter space, and the investigation of behaviors developing over timescales far too long to be accessible through the former. In both cases, the interaction between flow and field emerges as highly dynamical, with the cyclic evolution of the magnetic field impacting the flow as much as magnetically-mediated variations of the flow influence the evolution of the magnetic field.

The numerical results obtained in sections 3 and 4 using the dynamo-inspired LODM indicate that the nonlinear backreaction of the magnetic field on the meridional flow can cause large variations in the magnetic cycle's amplitude, including period doubling, chaos, and, in the presence of relatively low levels of stochastic forcing, multi-cycle amplitude modulation and intermittency. Even though the dynamo operating in the global MHD simulations investigated in section 2 is not a flux transport dynamo, one may legitimately ask whether variations of the meridional flow observed therein play a role in determining the amplitude of the magnetic cycles developing in these simulations.

We therefore return to the simulation results discussed in section 2, and now examine the energetics of the flow-field interaction. In the absence of Poynting flux

through the domain boundaries, the magnetic energy ε_B in a volume V varies in time according to

$$\frac{\partial \varepsilon_B}{\partial t} = -\int_V \mathbf{u} \cdot \mathbf{F} \, \mathrm{d}V - \int_V \frac{\mathbf{j}^2}{\sigma} \, \mathrm{d}V \ , \tag{8}$$

where $\mathbf{j}$ is the electric current density and σ is the electrical conductivity of the plasma. In practice, the second term on the r.h.s. corresponds to the Ohmic dissipation and will always contribute to the decrease of the magnetic energy. We are especially interested here in the first term of the r.h.s. of equation (8). This term represents the work done per unit time by the Lorentz force $\mathbf{F}$ on the velocity field $\mathbf{u}$, or vice versa: If $\mathbf{u} \cdot \mathbf{F}$ is positive, the magnetic field transfers energy to the flow, and if $\mathbf{u} \cdot \mathbf{F}$ is negative, the magnetic field gains energy from the flow. This quantity can be computed from the simulation output.

The results of calculating $\mathbf{F}$ and $\mathbf{u} \cdot \mathbf{F}$ in our simulation are presented in Figure 12. These meridional plane diagrams are constructed by first computing the $\mathbf{j} \times \mathbf{B}$ Lorentz force directly from the simulation output, computing $\mathbf{u} \cdot \mathbf{F}$ at every grid point on the 3D mesh, and then averaging zonally and temporally over the extent of the first six half-cycles in the simulation. The energy transfer term $\mathbf{u} \cdot \mathbf{F}$ embodies some important information specially when broken up into its three contributions in the zonal, latitudinal and radial directions (B through D on Figure 12). The radial and zonal contributions are negatively-signed throughout the domain, indicating average energy transfer from the associated flow components to the magnetic field. Physically, these distributions are dominated by the work done by the differential rotation shear ($U_\phi F_\phi$) and convective updrafts and downdrafts ($U_r F_r$) against the poloidal and toroidal magnetic components, respectively. However, the latitudinal contribution ($U_\theta F_\theta$) is almost everywhere positive, indicating magnetic driving of the latitudinal mean flow. The magnetic field thus extracts energy from rotation and differential rotation, and transfers part of this energy into the meridional flow via the Lorentz force associated with the dynamo-generated large-scale magnetic field. As can be inferred from Figure 12A, this transfer dominates the global energy flow between large scale flow and field at the base of the convecting layers, near the poles, and at mid-depth in the high-latitude portions of the convecting layers.

This simple energy analysis indicates that cyclic acceleration of the meridional flow acts as a sink of magnetic energy. This suggests that magnetically-driven modulation of the meridional flow contributes significantly to the amplitude saturation of the large-scale magnetic field building up these simulations. If this state of affairs were to carry over to the real sun, then some very fundamental working assumptions of many contemporary versions of flux transport dynamo models of the solar cycle must be called into question. In nearly all versions of these models that we are aware of, the large-scale magnetic field is passively advected by the flow; and, in particular for advection-dominated flux transport dynamo models relying on the Babcock-Leighton mechanism of poloidal field regeneration through the surface decay of active regions, the presence and continuous operation of this flow is essential to carry this poloidal component to the base of the convective envelope, where induction of the toroidal component is presumed to take place. At least in the few global MHD simulation we have analyzed in some detail as yet, the dynamical relationship between the meridional flow and large-scale magnetic field could not be farther from this simple kinematic picture, with the field driving the meridional flow at most depths and latitudes throughout the convectively unstable layers (Figure 12C). Nor can the

magnetic backreaction of the large-scale magnetic field on the meridional flow be reduced to a mere overall decrease of this flow's amplitude, as one may be tempted to infer from, e.g., the observational analysis of Hathaway and Rightmire (2010); instead, the backreaction shows a strong spatial dependency, as evidenced by the breakup of the primary large-scale flow cell in the descending phases of the cycle (Figure 4), and the presence of spatially extended regions where the meridional flow speed actually increases with increasing magnetic field strength (Figure 2), as well as overall cycle amplitude (Figure 3).

On the other hand, the analysis of §3, based on LODM reduction of the axisymmetric mean-field dynamo equations, suggests that the interplay between the meridional flow and large-scale magnetic can lead to very rich dynamical behavior, including amplitude modulation, period doubling, chaos, and even intermittency. The global MHD simulations analyzed in §2 span only six half-cycles, which is of course far too short to be able to identify unambiguously counterparts of these behaviors; yet the strong positive correlation found between the mid-latitude meridional flow speed at the core-envelope interface and toroidal field strength measured at the same location, (Figure 3D) is consistent with the behavior observed in the LODM.

Recent observational analyses of the meridional flow at the solar surface over timescales decadal and up have revealed a modulation in antiphase with the sunspot cycle, with the development of a secondary, counterrotating flow cell at high latitudes. While some controversy remains regarding what the various data analyses techniques are really measuring, the fact that very similar modulation patterns also arise in our global MHD simulations suggests that in the sun these are also ultimately powered by the dynamo-generated large-scale magnetic field. Such a modulation can be driven directly by the Lorentz force, and/or indirectly via magnetic driving of torsional oscillations, as is indeed observed in the simulations analyzed here (Beaudoin et al. 2012, in preparation). Cyclic variations in the meridional flow may therefore hold important clues regarding the manner in which this dynamo operates, and most importantly perhaps, on what drives the cycle-to-cycle variations in amplitude and duration.

References

Basu, S., Antia, H. M.: 2010, *Astrophys. J.* **717**, 488.
Beaudoin, P., Charbonneau, P.: 2011 *in preparation.*
Beer, J., Tobias, S.M., Weiss, N.: 1998, *Solar Phys.* **181**, 237.
Braun, D.C., Fan, Y.: 1998, *Astrophys. J. Lett.* **508**, L105.
Brooke, J., Moss, D., Phillips, A.: 2002, *Astron. Astrophys.* **395**, 1013.
Brun, A.S., Miesch, M.S., Toomre, J.:2004, *Astrophys. J.* **614**, 1073.
Bushby, P.J.: 2006, *Mon. Not. Roy. Astron. Soc.* **371**, 772.
Bushby, P.J., Tobias, S.M.: 2007, *Astrophys. J.* **661**, 1289.
Charbonneau, P.: 2010, *Living Rev. Solar Phys.* **7**, 3, (cited on 10/2011): http://www.livingreviews.org/lrsp-2010-3 .
Charbonneau, P., Dikpati, M.: 2000, *Astrophys. J.* **543**, 1027.

Charbonneau, P., Smolarkiewicz, P.K., *J. Comp. Phys.*, submitted (2011)

Chatterjee, P., Nandy, D., Choudhuri, A.R.: 2004, *Astron. Astrophys.*, **427**, 1019.

Dikpati, M., Gilman, P.A., de Toma, G., Ulrich, R.K.: 2010, *Geophys. Res. Lett.* **37**, L14107.

Fröhlich, C.: 2011, *Space Sci. Rev.* **724**, 2, 1021.

Ghizaru, M., Charbonneau, P. and Smolarkiewicz, P.K.: 2010, *Astrophys. J. Lett.* **715**, 133.

González Hernández, I., Komm, R., Kholikov, S., Howe, R., Hill, F.: 2011, JPhCS, **271**, 012073.

Howe, R., Hill, F., Komm, R., Christensen-Dalsgaard, J., Larson, T.P., Schou, J., Thompson, M.J., Ulrich, R.K.: 2011, JPhCS, **271**, 012074.

Hathaway, D., Rightmire, L.: 2010, *Astrophys. J.* **729**, 80.

Jiang, J., Cameron, R., Schmitt, D., & Schüssler, M.: 2009, *Astrophys. J. Lett.* **693**, L96.

Karak, B.: 2010, *Astrophys. J.* **724**, 2, 1021.

Karak, B., Choudhuri, A.R.: 2011, *Solar Phys.*, accepted.

Kitchatinov, L.L., Mazur, M.V., Jardine, M.: 2000, *Astron. Astrophys.* **359**, 531.

Lopes, I., and Passos, D.: 2009, *Solar Phys.* **257**, 1.

Miesch, M.S., Toomre, J.: 2009, *Ann. Rev. Fluid Mech.* **41**, 317.

Moss, D., Brooke, J.M.: 2000, *Mon. Not. Roy. Astron. Soc.* **315**, 521.

Nandy, D., Muñoz-Jaramillo, A., Martens, P.C.H.: 2011, *Nature* **471**, 80.

Passos, D., Lopes, I.P.: 2008, *Astrophys. J.* **686**, 2, 1420.

Passos, D., Lopes, I.P.: 2011 *J. Atmos. Sol. Terr. Phys.* **73**, 191.

Passos, D.: 2011, *Astrophys. J.*, in press.

Pontieri, A., Lepreti, F., Sorriso-Valvo, L., Vecchio, A., Carbone, V.: 2003, *Solar Phys.* **213**, 195.

Racine, E., Charbonneau, P., Ghizaru, M., Bouchart, A., Smolarkiewicz, P.K.: 2011, *Astrophys. J.* **735**, 22.

Rempel, M.: 2006, *Astrophys. J.* **647**, 662.

Tapping, K.F., Valdés, J.J.: 2011, *Solar Phys.* **272**, 337.

Tobias, S.M.: 1996, *Astrophys. J.* **467**, 870.

Ulrich, R.K.: 2010, *Astrophys. J.* **725**, 658.

White, O.R., Kopp, G., Snow, M., Tapping, K.F.: 2011, *Solar Phys.* , 142.

(A) $B_\phi(r,\theta)$

(B) $U_\phi(r,\theta)/r\cos(\theta)$

(C) $U_\theta(r,\theta)$

(D) $U_r(r,\theta)$
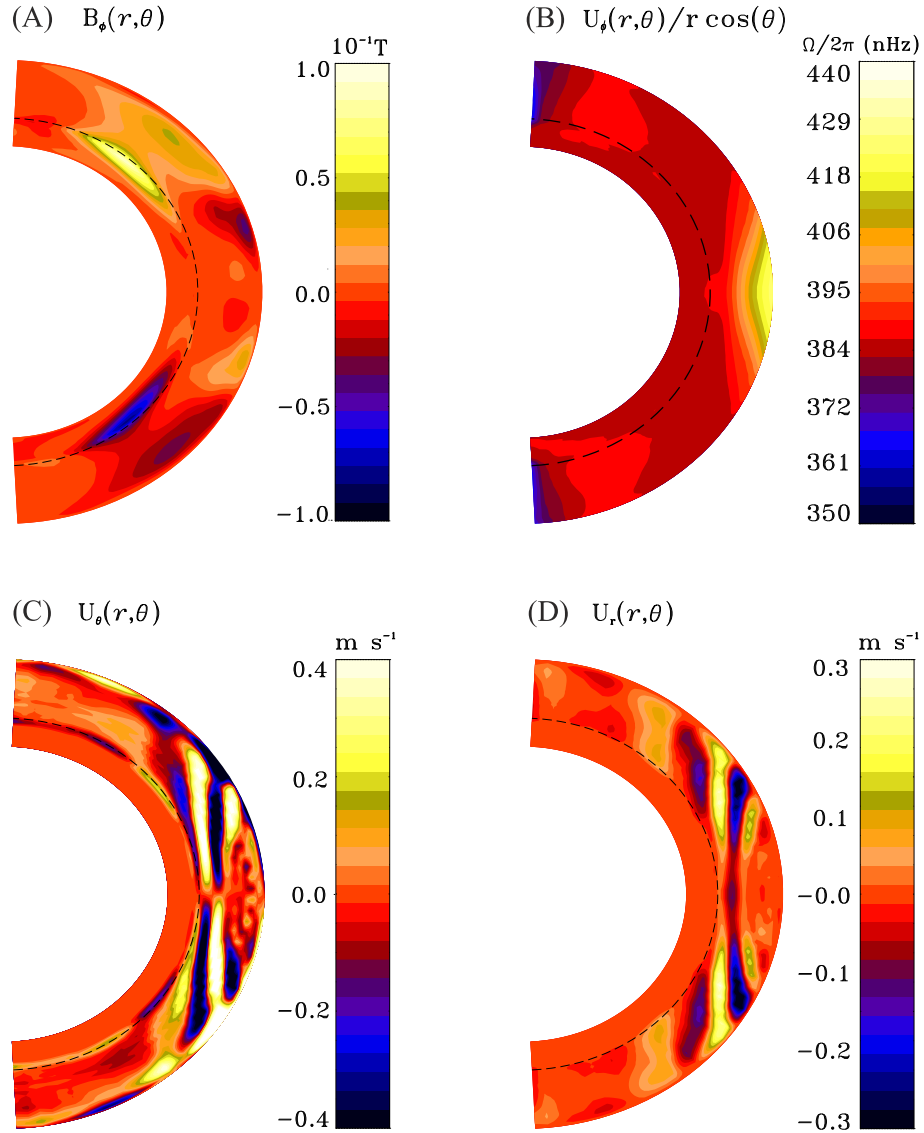
Figure 1. Longitudinal means of various quantities extracted from the simulation output, and temporally averaged over 3 cycles of the same magnetic polarity (cycles 1, 3 and 5). Panel (A) presents B_ϕ while panels (B), (C) and (D) show rotational frequency ($\Omega/2\pi = U_\phi/r\cos\theta$), U_θ and U_r respectively. The color scales for U_θ and U_r are slightly saturated to show more detail. All quantities are plotted in meridional planes, over a depth range $0.62 \leq r/R_\odot \leq 0.96$. The rotation axis oriented vertically, and the latitudinal variable θ ranging from -90° south to 90° north. The U_θ component is measured in relation to the south pole, i.e., positive values correspond to Northward motions and negative values to Southward motions. The dashed circular arc indicates the base of the convectively unstable layers in the simulation.
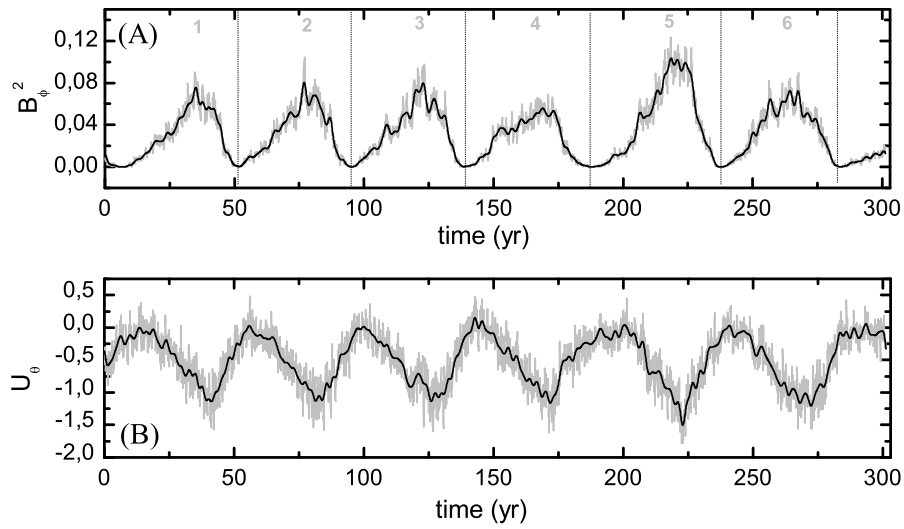
Figure 2. In panel (A) we present B_ϕ^2 (in Tesla square) evolution over the simulation period (in gray). The thick black line is a smoothed version obtained with a FFT low pass filter of width 1 year. Panel (B) shows U_θ (in m s^{-1}), for the same period. Again, the thick black line results form a 1 year low pass filter of the original simulation data, in gray. These two quantities are sampled at the base of the convecting layers ($r/R = 0.718$) and at 58° north. Individual half-cycles are delineated from one minimum in the B_ϕ^2 time series to the next, as indicated by the dotted lines, and numbered for future reference.
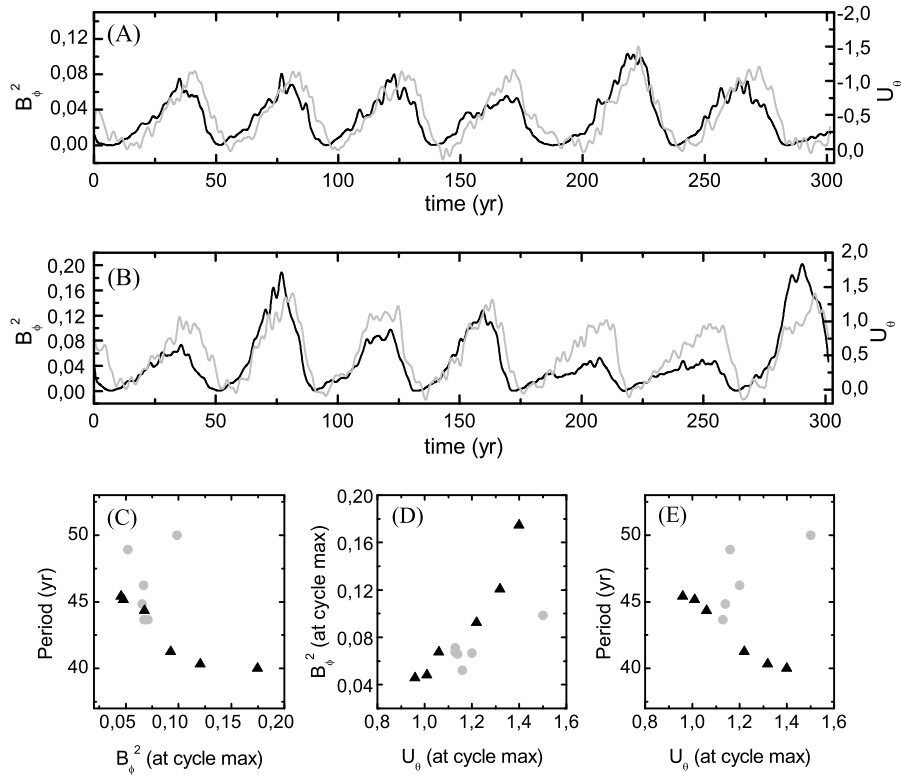
Figure 3. In panel (A) we show the evolution of the smoothed squared toroidal field (black) and the meridional flow (U_θ in gray) measured at tachocline depth near 58 degrees north. The same quantities measured at 58 degrees south at tachocline depth are shown in panel (B). In the bottom row, we have in panel (C) the cycle amplitude represented by B_ϕ^2 at cycle peak vs cycle period (linear correlation coefficient $r = -0.58$), in panel (D) the peak amplitude of the meridional flow vs cycle amplitude ($r = 0.78$), and in panel (E) the peak amplitude of the meridional flow vs cycle period ($r = -0.04$). In all cases black triangles indicate values measured at 58 degrees South while gray circles represent values measured at 58 degrees North.
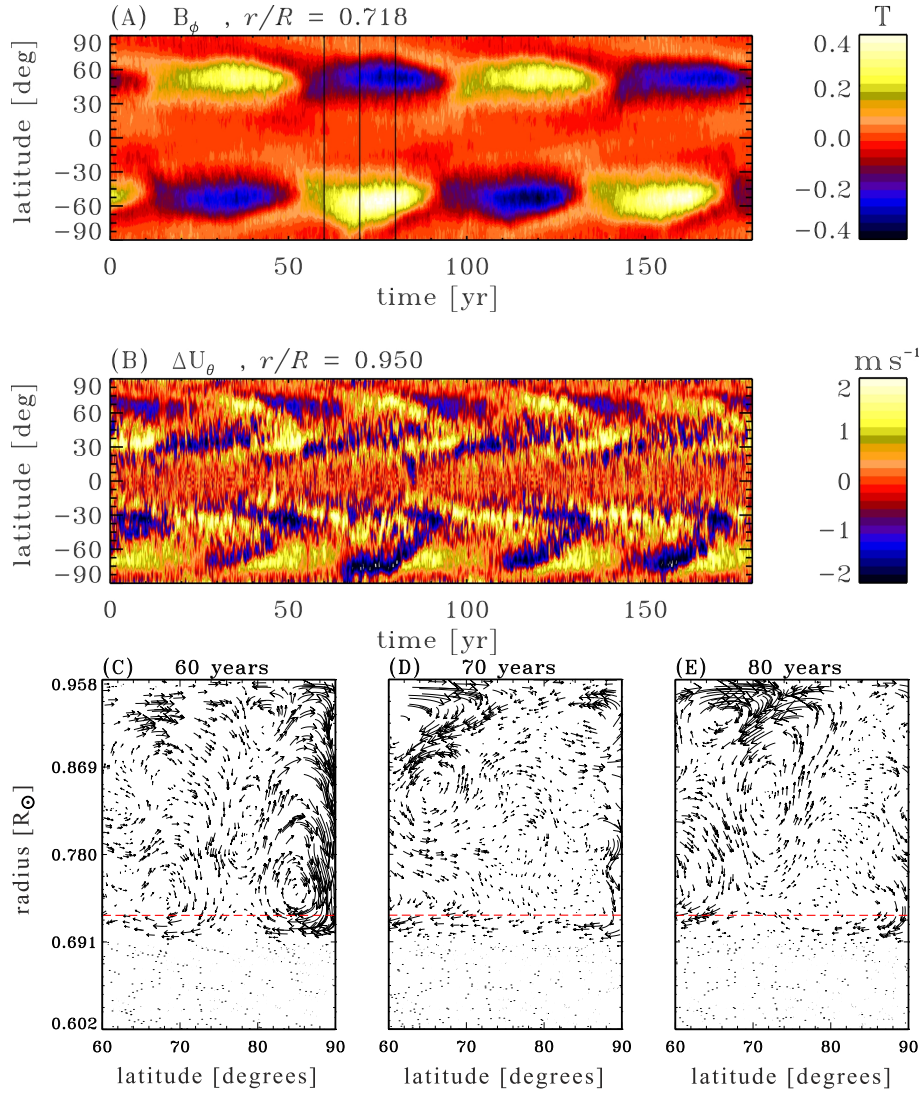
Figure 4. Development of secondary, high-latitude counterrotating meridional flow cells in the same simulation used to produce Figures 1, 2 and 3. Panel (A) shows a time-latitude diagram of the zonally-averaged large-scale toroidal magnetic component at the core-envelope interface ($r/R = 0.718$), the simulation's equivalent of the sunspot butterfly diagram. Panel (B) shows the surface latitudinal velocity residual obtained by subtracting the zonal and temporal mean of this flow component from the simulation output. Panels (C) through (E) show meridional flow vectors in the vicinity of the N-pole in a cartesian latitude-radius plot, uniformly spaced across the second magnetic half-cycle of panel (A) at times indicated therein by vertical line segments. The horizontal dashed line indicates the core-envelope interface.
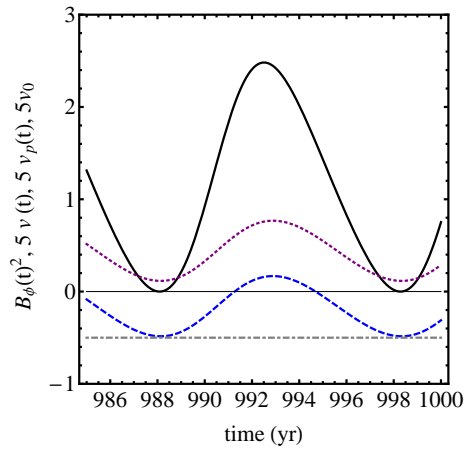
Figure 5. Comparison between the toroidal field (black thick line), v_p (dashed blue line), $v(t)$ (purple dotted line) and v_0 (gray dot-dashed line) for a standard solution. Here the values of the flow are multiplied by a factor of 5 so as to be visible on the scale of B_ϕ^2.
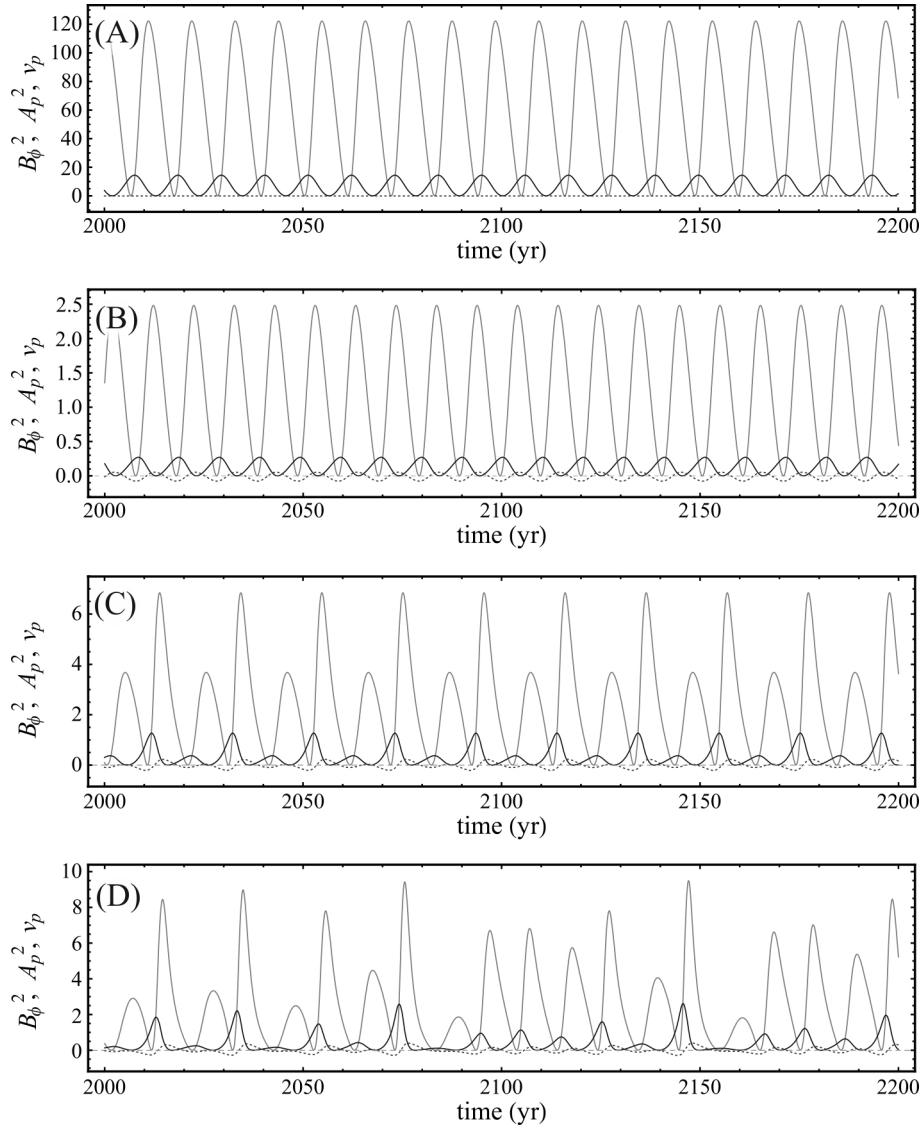
Figure 6. Example of solutions for equations (2) and (3) under different feedback parameters. In light gray we have B_ϕ^2, in black A_p^2 and the dashed gray line represents v_p. All solutions were generated using $c_1 = -0.01$, $c_2 = 0.95$, $c_3 = 0.002$, $\alpha = -0.1$. In panel (A) is presented a kinematic reference solution produced by enforcing $v(t) = 0$ at all times, with $v_0 = -0.1$, $a = b = 0$; (B) shows a regular cyclic non-kinematic solution, with $v_0 = -0.1$, $a = 0.1$, $b = 0.05$; (C) presents a solution displaying period doubling, obtained using $v_0 = -0.1$, $a = 0.1$, $b = 0.25$. Panel (D) shows a solution in the chaotic regime, with $v_0 = -0.13$, $a = 0.1$, $b = 0.25$.
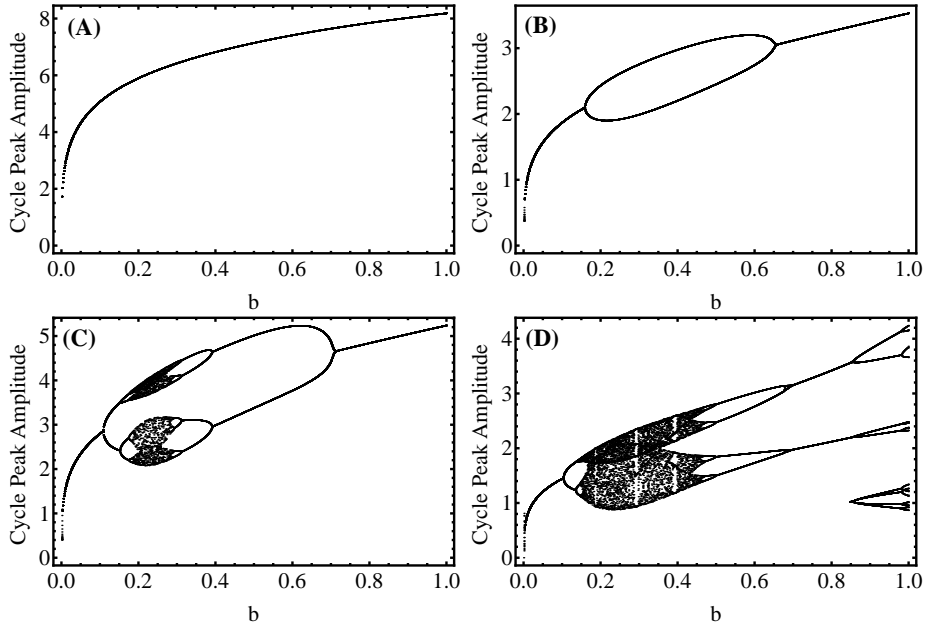
Figure 7. Bifurcation maps for maximum amplitude of the toroidal field (equivalent to solar cycle maximum) obtained by varying b between 10^{-4} and 1 for different a and v_0. (A) Single period regime, $v_0 = -0.1$, $a = 0.01$. (B) Appearance of period doubling, $v_0 = -0.1$, $a = 0.1$. Panels (C) and (D) show signatures of chaotic regimes with multiple attractors and windows, obtained with $v_0 = -0.13$, $a = 0.05$ and $v_0 = -0.13$, $a = 0.2$ respectively. Bifurcation and chaos are common in this model's parameter space, but the size and shape of chaotic windows can vary significantly in different regions.
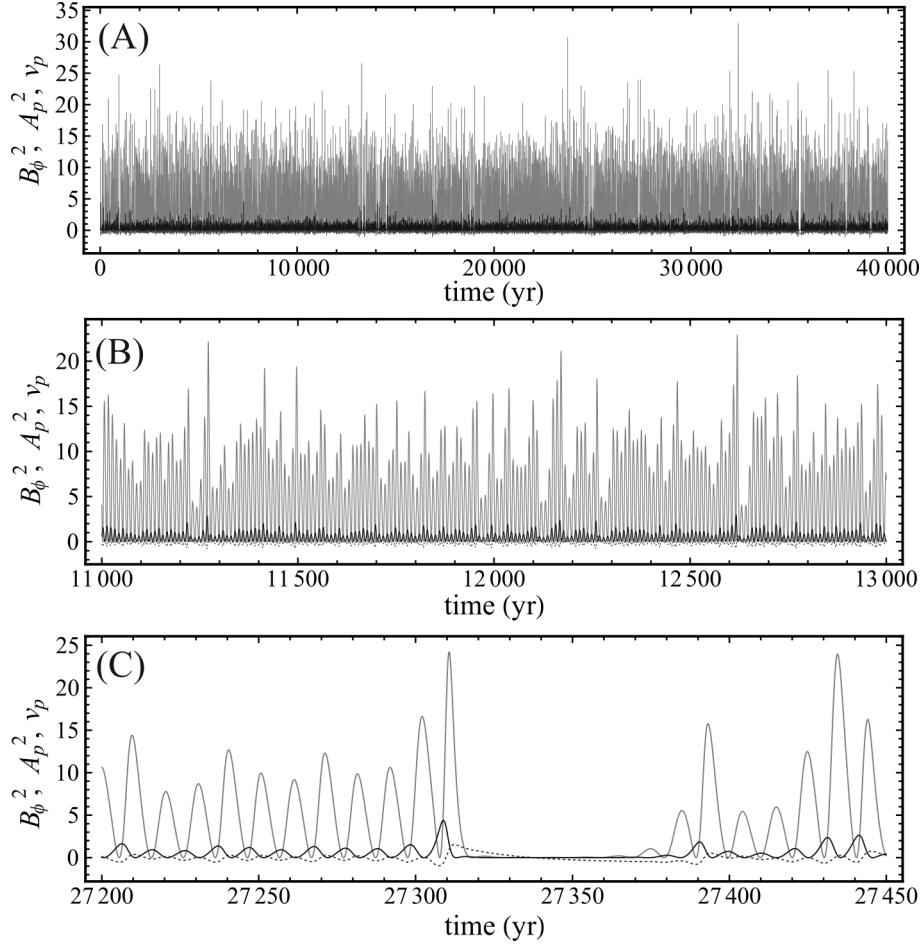
Figure 8. Simulation results for fluctuating $a \in [0.01, 0.03]$, $b = 0.05$ and $v_0 = -0.11$. All other model parameters are the same as in the reference solution. Panel (A) shows $B_\phi^2(t)$ (light gray) and $A_p^2(t)$ (black) for 40000 years simulation. Panel (B) is a zoom in to show a section of the simulation where the long term modulation can be seen. In light gray is $B_\phi^2(t)$, black $A_p^2(t)$ and a scaled version of the meridional flow, in this case $5 \times v_p(t)$ is presented as a gray dashed line. In panel (C) the same quantities but this time zooming in into a grand minimum (off phase) period.
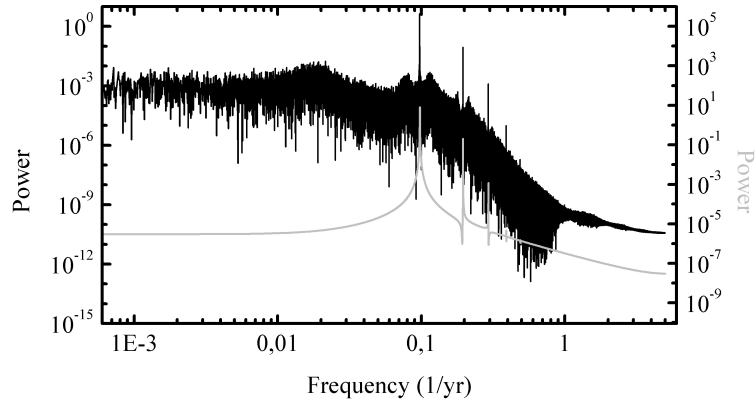
Figure 9. Power spectrum of a 240000 yr long extension of the simulation plotted on Figure 8 (in black). The peak amplitude is found around 10.2 years, with harmonics at 5.2, 3.4 and 2.6 years. On the low band of the spectrum, we have a broad bump centered around 56 years. The power spectrum in gray is that associated with a parent solution using the same parameter values but not subjected to stochastic forcing, plotted on a different scale (on the right) to ease comparison.
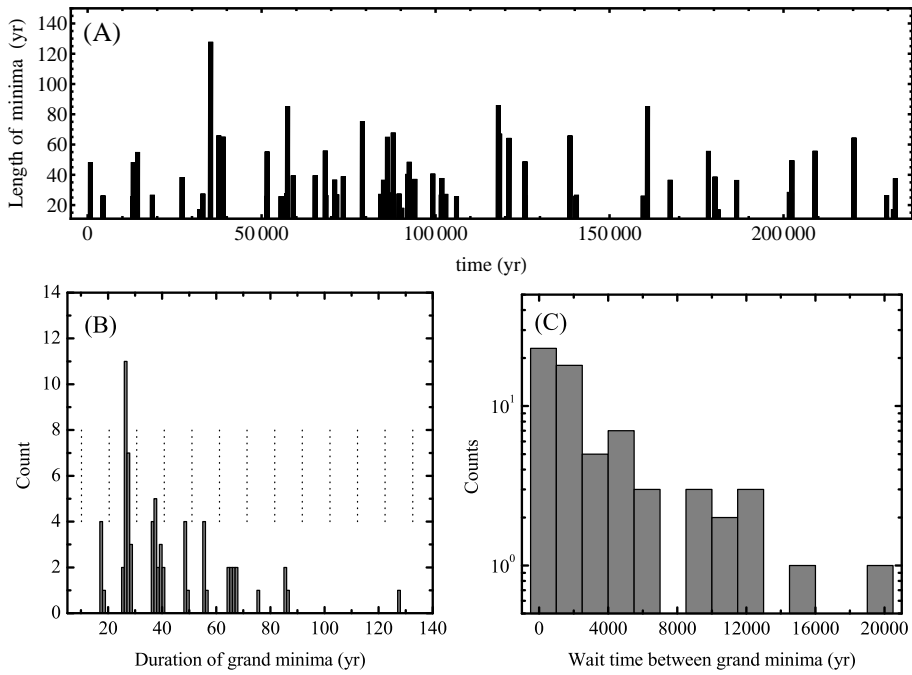
Figure 10. Panel (A) indicates the times of occurrence of grand minima (black bars) and their duration in years. The corresponding histogram is presented in panel (B) using 1 yr bins. The vertical dotted lines are references at multiples of the base period of 10.2 yr. In panel (C) is displayed the histogram of the duration of normal cyclic activity phases between grand minima, in 1500 yr bins.
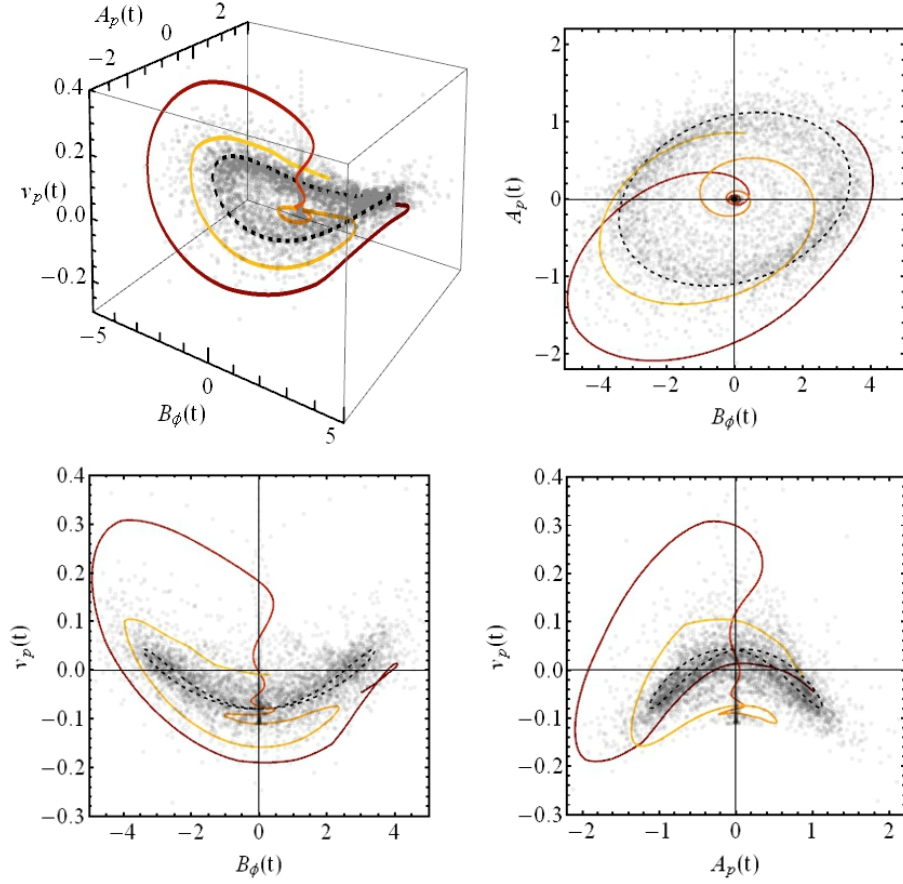
Figure 11. Phase spaces of a solution with stochastic forcing of the Lorentz force parameter a, here with amplitude $\Delta a/a = 0.5$. The gray dots represent 1 year intervals between t=35000 and t=40000. The colored line shows the trajectory in and out of a grand minimum (starting from dark red, t=27300 and ending in yellow, t=27400 (cf. Fig. 8C). The black dashed line represents the trajectory of an unperturbed solution with $a = 0.02$.
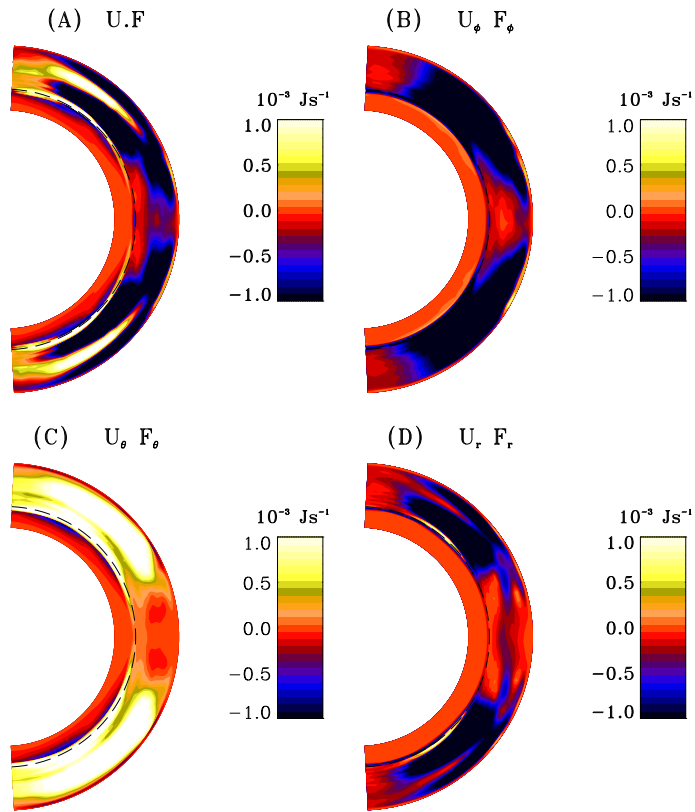
Figure 12. Meridional plane representation of the zonal and temporal average of $\mathbf{u} \cdot \mathbf{F}$ (panel A), together with the individual contributions from the three coordinate directions in panels B through D. The dashed circular arc indicates the base of the convectively unstable layers in the simulation.